Chapter 6

HA nanoplates as a novel antibiotic drug vehicle

The current chapter explores the antibacterial potential of antibiotic-loaded HA nanoplates with detailed study of their drug loading and release behavior as compared to HA nanorods. Doxycycline hyclate (DOX) is selected as a model antibiotic drug for its potent antibacterial response against both, gram-negative and gram-positive bacteria. The successful loading of DOX onto HA nanocrystals is validated through XRD, FTIR, and electron microscopies. Moreover, the nature of the interaction between DOX and differently-shaped HA nanocrystals is revealed using XPS analyses. The in vitro release dynamics of DOX from DOX-HA nanocrystals were evaluated as per the varying morphology of HA nanocrystals. Further, in vitro cell culture and hemolysis assays are conducted to assess the biocompatibility, including cell viability and hemocompatibility of DOX-HA nanocrystals. Finally, the impact of the sustained release of DOX from DOX-HA nanocrystals on antibacterial efficacy has also been thoroughly examined and compared with pure DOX.

6.1. Drug loading response: Role of morphology

Fig. 6.1A depicts the drug loading efficiency of HA nanocrystals, HA nanorods, nanoplates, and thin nanoplates, calculated using the equation (2.6) and DOX standard concentration curve (Fig. 6.1 B). It can be clearly seen that the HA thin nanoplates loaded the highest amount of DOX drug (73.3 %) than HA nanoplates and nanorods with DOX loading efficiency of 62.2 and 45.5 %, respectively. The successful loading of DOX on the surface of HA nanocrystals and significant variation in DOX loading percentage as per their morphology was assessed using FTIR spectroscopy, XRD technique, FESEM, and TEM.

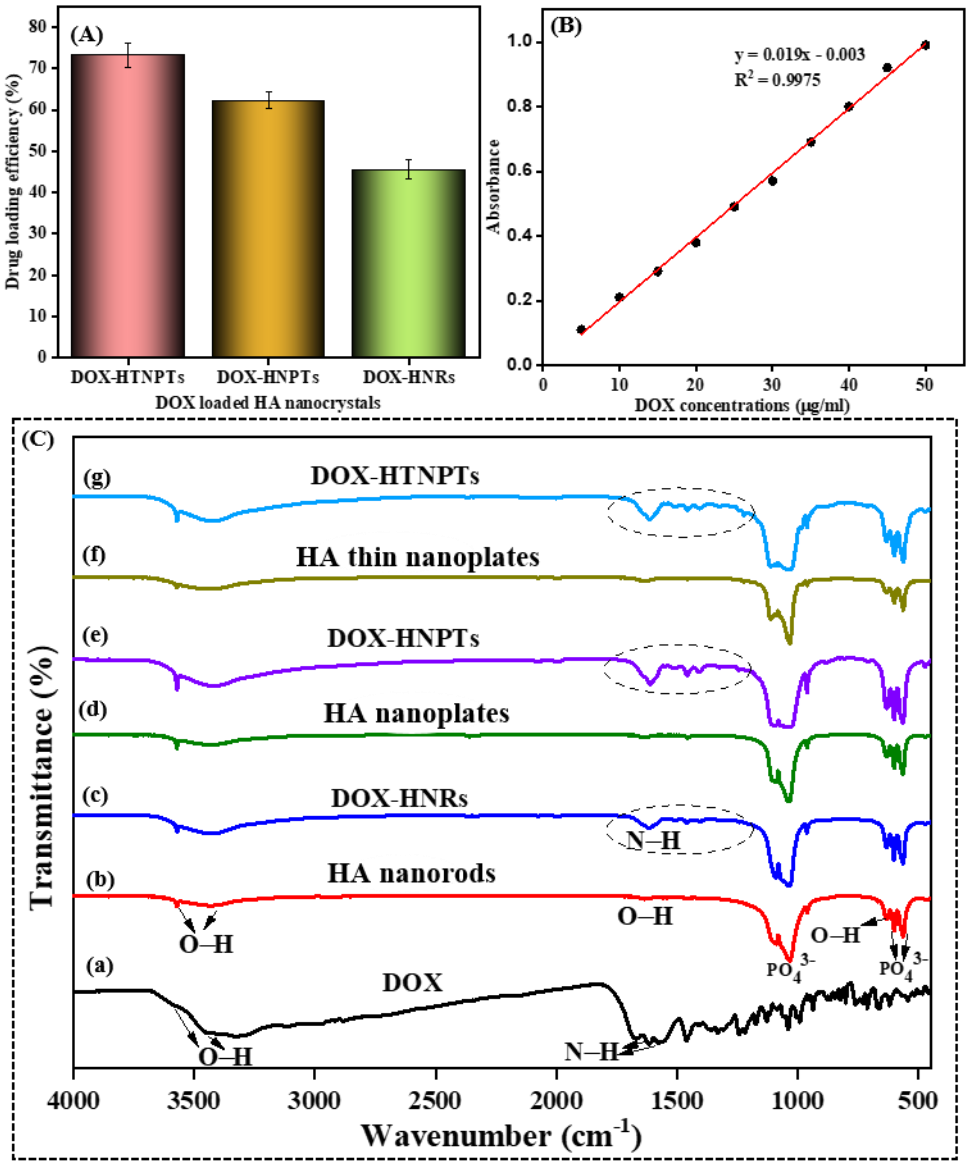

Figure 6.1. *(A) The bar plot, representing the DOX loading efficiency of HA nanorods, nanoplates, and thin nanoplates. Value of standard deviation was derived from three independent experiments, at $p \leq 0.05$. (B) Standard DOX curve across the concentration range of 5 - 50 µg/ml, plotted at the wavelength of 350 nm, and (C) FTIR spectra of HA nanocrystals before (HA nanorods, nanoplates, and thin nanoplates) and after DOX loading [DOX-loaded HA nanorods (DOX-HNRs), DOX-loaded HA nanoplates (DOX-HNPTs), DOX-loaded HA thin nanoplates (DOX-HTNPTs)].*

6.1.1. FTIR and XRD: Drug loading evidence

The successful loading of DOX was confirmed by investigating their functional groups on FTIR spectra of DOX-loaded HA nanocrystals. Fig. 6.1C shows the FTIR spectra of HA nanorods, nanoplates, and thin nanoplates before and after loading of DOX drug. In pure HA nanocrystals [Fig. 6.1C (b, d and f)], the vibrational bands between 3300 - 3600 cm^{-1} can be assigned to the stretching vibration of O-H group, present in HA nanocrystals [1]. After DOX loading, these bands became more pronounced, as clearly visible in Fig. 6.1C (c, e and g). This observation may be attributed to the incorporation of O-H groups of DOX molecules, as confirmed by FTIR spectra of pure DOX [Fig. 6.1 C (a)]. Unlike pure HA nanocrystals, new vibrational peaks also appeared between 1684 – 1205 cm^{-1} in the spectra of DOX-loaded HA nanorods (DOX-HNRs), DOX-loaded HA nanoplates (DOX-HNPTs), and DOX-loaded HA thin nanoplates (DOX-HTNPTs), which correspond to N-H and -CH_2 vibrations in DOX molecules. Specifically, the absorption bands at 1610 and 1570 cm^{-1} were ascribed to amide (I and II) groups [2], overlapped with the bending vibration of O-H group (1635 cm^{-1}), present in HA nanocrystals. The respective peaks at 1458 and 1326 cm^{-1} were caused by asymmetric and symmetric bending modes of the -CH_2 group. The vibrational band at 1243 cm^{-1} can be associated to the C-O bond [3]. Finally, FTIR analyses verify the successful loading of DOX on the surface of HA nanocrystals.

XRD data were also recorded to investigate the impact of loaded DOX on the phase and crystallinity of HA nanocrystals. Fig. 6.2 shows the XRD patterns of HA nanorods, nanoplates, and thin nanoplates before and after loading of DOX. The incorporation of DOX significantly reduced the crystallinity of HA nanocrystals [Fig. 6.2A (b, d and f)]. The degree of crystallinity of HA nanorods, nanoplates, thin nanoplates and DOX-HNRs, DOX-HNPTs, DOX-HTNPTs was calculated to be (89, 97, 86 %) and (80, 84, 76 %), respectively. It further reveals the molecular interaction of DOX with HA nanocrystals. Most of the diffraction peaks in DOX-

HNRs, DOX-HNPTs and DOX-HTNPTs are similar to those of indexed peaks (JCPDS number: 09-0432) of pure HA, indicating no change in the hexagonal phase of HA nanocrystals. However, additional peaks appeared at 27.75° and 34.30° in the XRD pattern of DOX-HTNPTs, as can be seen in Fig. 6.2B (f), which may be attributed to the peaks of DOX molecules. It verifies the highest drug loading efficiency of HA thin nanoplates, as no new peaks was observed in the XRD pattern of DOX-HNRs, DOX-HNPTs.

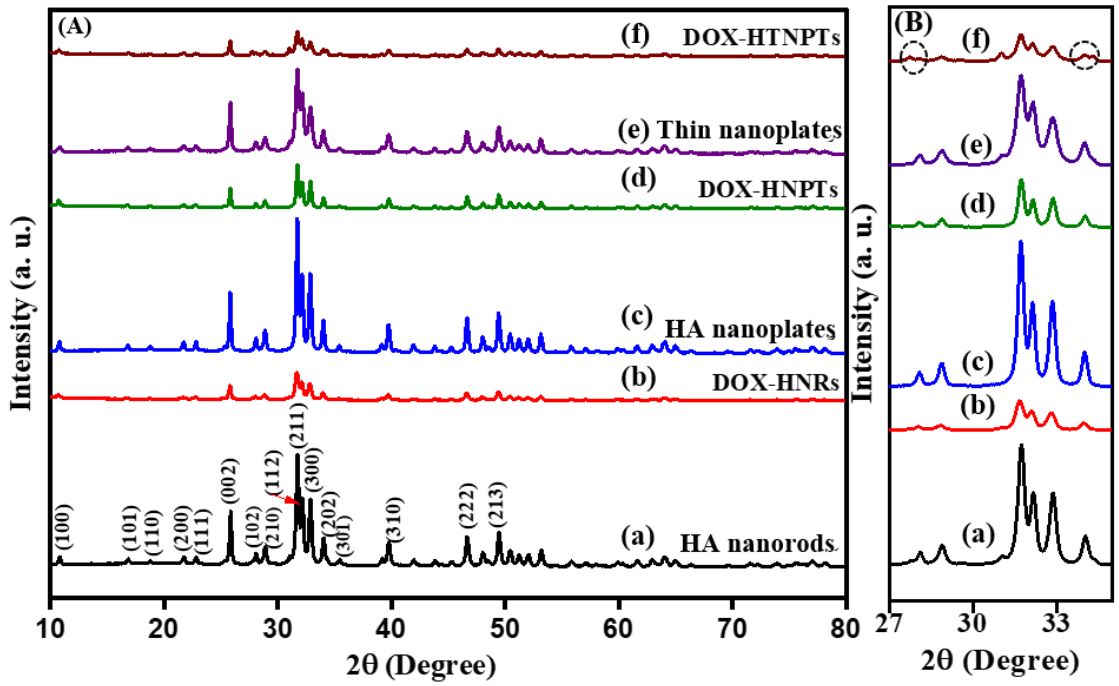

Figure 6.2. *XRD pattern of HA nanocrystals before (HA nanorods, nanoplates, and thin nanoplates) and after DOX loading (DOX-HNRs, DOX-HNPTs, DOX-HTNPTs) (A) and their enlarged view (B)*

6.1.2. SEM and TEM: Morphological changes

The morphological characteristics of DOX-loaded HA nanocrystals were also characterized using TEM and FESEM. Fig. 6.3A shows the bright field TEM images of HA nanorods, nanoplates, and thin nanoplates before and after loading of DOX. As compared to clear and sharp morphology of HA nanorods and nanoplates [Fig. 6.3A (a1, b1)], DOX-HNRs, DOX-HNPTs display agglomerated NPs, due to which clear visibility of shapes of HA nanocrystals

have been disappeared [Fig. 6.3A (a2, b2)] On the other hand, discrete HA thin nanoplates [Fig. 6.3A (c1)] are stacked to each other in DOX-HTNPTs along with intercalated DOX, as clearly observed in Fig. 6.3A (c2). It might be responsible for higher drug loading on HA thin nanoplates as compared to HA nanorods and nanoplates. The morphological changes also investigated through FESEM. The discrete particles of HA nanorods, nanoplates, and thin nanoplates [Fig. 6.3B (a1, b1, and c1)], are compacted due to the incorporation of DOX, as clearly visible Fig. 6.3B (a2, b2, and c2).

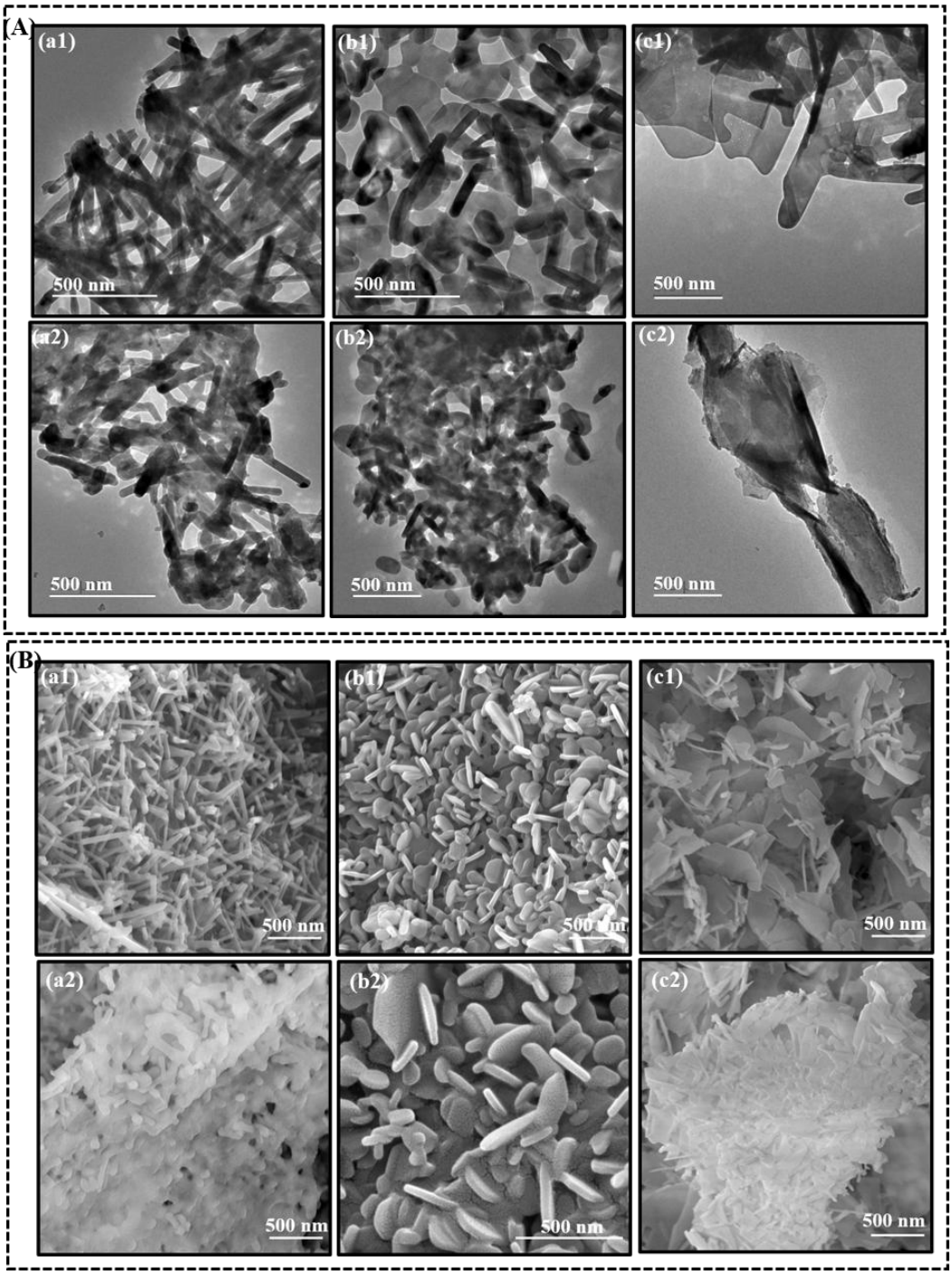

Figure 6.3. *TEM (A) and FESEM (B) images of different-shaped HA nanocrystals before; HA nanorods (a1), nanoplates (b1), and thin nanoplates (c1), and after loading of DOX; DOX-HNRs (a2), DOX-HNPTs (b2), DOX-HTNPTs (c2)*

6.1.3. XPS analyses: Interaction between HA and DOX

The nature of interaction between HA and DOX was analyzed using XPS. Fig. 6.4 depicts the high resolution individual core level spectra of Ca 2p, P 2p, and O 1s orbitals of HA

nanocrystals before and after loading of DOX drug. Ca 2p and P 2p were fitted with two deconvoluted peaks, $2p_{1/2}$ and $2p_{3/2,}$ and O 1s spectra was fitted with two peaks, related to lattice oxygen (O_L) of P–O bond and oxygen (O_H) of O–H bond [4]. A visible shift in their peaks after loading of DOX on HA nanorods, nanoplates, and thin nanoplates was observed. In case of HA nanorods after loading of DOX, the binding energy (B.E.) of both, Ca 2p and P 2p peaks was shifted to lower value; 350.38 - 350.34, 346.84 - 346.80 eV for Ca $2p_{1/2}$, Ca $2p_{3/2}$, and, 133.62 - 133.42, 132.69 - 132.56 eV for p $2p_{1/2}$, P $2p_{3/2}$, respectively [Fig. 6.4 A (a, b)]. In contrast, O 1s peaks shifted to higher energy value, i.e., 530.76 - 530.81 eV for O_L peak and 532.13 - 532.23 eV for O_H peak [Fig. 6.4A (c)]. Such variation in B.E. reveals the hydrogen-bonding interaction of HA nanorods with DOX molecules [5]. The O atoms of Ca-O, P-O and O-H groups, present in HA, partially donated electrons to H atoms of -OH and $-NH_2$ functional groups in DOX, forming H-bonds. Consequently, the electron density around O atoms of Ca-O, P-O and O-H bonds reduced. Therefore, core-level electrons of O are held more tightly to the nucleus, leading to an increase in their binding energy [Fig. 6.4 A (c)] [6] [7]. However, the reduced electron density around O atoms weakened the Ca-O and P-O bonding. Thereby, the binding energy of Ca 2p and P 2p decreases [Fig. 6.4A (a, b)] [8]. On the other hand, DOX loading on HA nanoplates and thin nanoplates shifted the binding energy of Ca 2p and P 2p to a higher value [Fig. 6.4 B (a, b) and C (a, b)]. This suggests the primary bonding interaction of Ca and P atoms with O atoms (of C=O, $CONH_{2,}$ and OH groups) of DOX [5, 9]. The shifting of O 1s peaks to higher B.E. reveals the formation of H-bond (secondary bond) with HA and DOX [Fig. 6.4 B (c) and C (c)]. Clearly, the predominant nature of the interaction of DOX on the surface of HA nanorods is weak H-bonding. In contrast, both, primary and secondary bonding are involved in the loading of DOX on the surface of HA nanoplates and thin nanoplates. This significant variation in the nature of interaction of DOX as per different shapes of HA nanocrystals is related to their surface area, which was calculated to be 18, 25.5 and 34

m^2/g for HA nanorods, nanoplates, and thin nanoplates, respectively. Due to lower surface area, HA nanorods possess fewer number of reactive sites than HA nanoplates and thin nanoplates, allowing major amount of drug loading through H-bonding interaction (lower energy is required to form). On moving from HA nanorods to nanoplates, number of reactive sites increases. It facilitates DOX loading through both, primary and secondary bonding. Owing to the highest surface area, HA thin nanoplates loaded even more amount of DOX through primary bonding along with reduction in DOX loading through secondary bonding, as confirmed by larger shift of Ca 2p (Δ B.E. = 0.11 eV for $2p_{1/2}$ and 0.10 eV for $2p_{3/2}$) and P 2p peaks (Δ B.E. = 0.17 eV for $2p_{1/2}$ and 0.15 eV for $2p_{3/2}$), and lesser shift of O 1s peak (Δ B.E. = 0.10 eV for O_L and 0.17 eV for O_H) to higher B.E. value as compared to HA nanoplates. The shift in B.E. of Ca 2p, P 2p and O 1s for HA nanoplates is Δ B.E. = 0.04 eV for Ca $2p_{1/2}$ and 0.06 eV for Ca $2p_{3/2}$; Δ B.E. = 0.14 eV for P $2p_{1/2}$ and 0.11 eV for P $2p_{3/2}$; Δ B.E. = 0.14 eV for O_L and 0.19 eV for O_H).

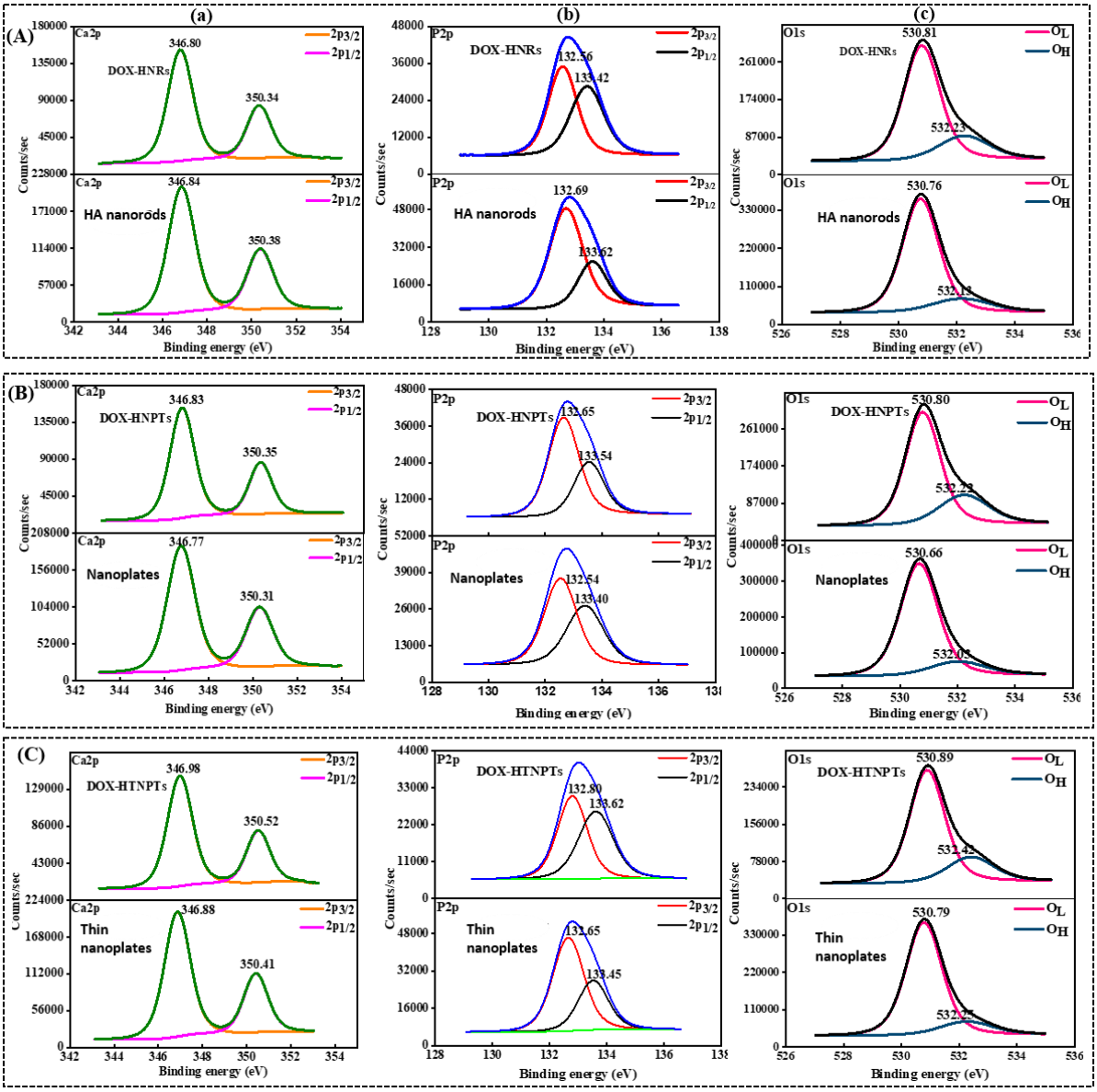

Figure 6.4. *XPS spectra of Ca 2p, P 2p and O 1s for HA nanorods and DOX-HNRs (A), HA nanoplates and DOX-HNPTs (B), and HA thin nanoplates and DOX-HTNPTs (C).*

6.2. *In vitro* drug release

To optimize therapeutic efficacy and reduce side effects, controlled drug release is essential for maintaining an ideal drug concentration at infection site. 10 wt.% of DOX was loaded into HA nanocrystals (HA nanorods, nanoplates, and thin nanoplates) using the solution route. The DOX release response from HA nanocrystals was examined in PBS (pH 7.4) at 37°C (Fig. 6.5 A). The DOX loaded in HA nanorods released 63 % within 8 h (burst release), then sustained release up to (plateau region) 48 h was observed. In contrast, significant sustained release of

DOX is observed in case of HA nanoplates and thin nanoplates. Specifically, 57 and 47 % of DOX released from HA nanoplates and thin nanoplates within 8 h (burst release) and sustained up to 48 h (Fig. 6.5A). There are number of critical factors that affect the drug release rate from HA nanocrystals, including DOX dissolution, solvent penetration, and DOX diffusion. The burst release of DOX (within 8 h) is result of weak secondary bonding (Hydrogen bonding/Van der waals), which is the most predominant in HA nanorods and the least predominant in HA thin nanoplates. The primary bonding interaction (Covalent/ionic) between HA nanocrystals and DOX facilitates prolonged and sustained release profile beyond 8 h. Moreover, higher controlled release of DOX from HA thin nanoplates can also be the result of delayed drug diffusion due to the intercalated DOX among thin nanoplates.

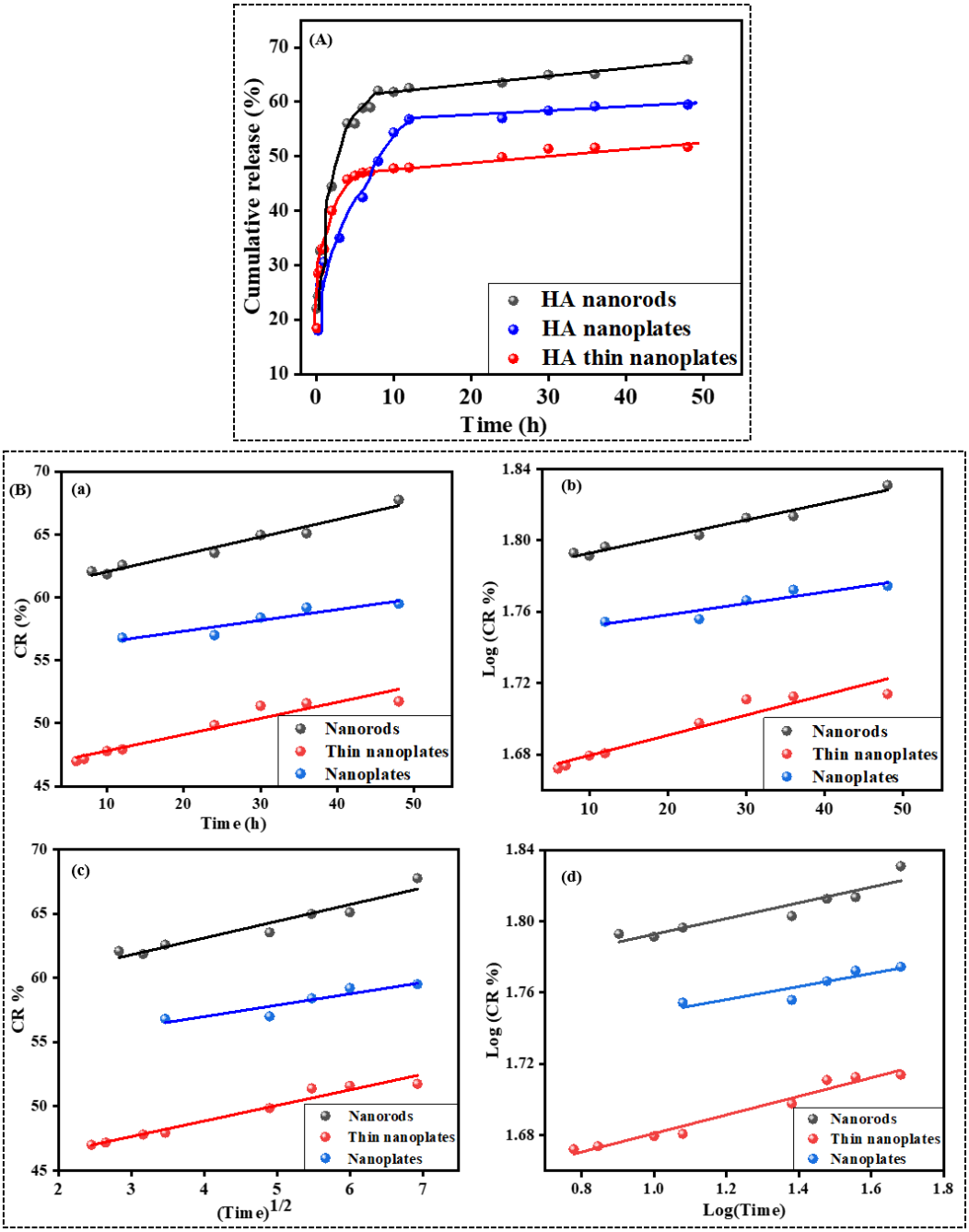

Figure 6.5 *(A) In vitro cumulative DOX release profile for HA nanorods, nanoplates, and thin nanoplates, and their DOX release kinetics models (B): zero order (a), first order (b), Higuchi model (c), and KP model (d).*

To better understand the drug release mechanism, various kinetic models were used to analyze the release profiles. Among them, the Higuchi model demonstrated the best fit, showing a high linear correlation coefficient ($r^2 \sim 0.96$) with exponent (k) values of 1.3, 0.9, and 1.2 for HA nanorods, nanoplates, and thin nanoplates, respectively (Table 6.1). Other kinetic analyses,

such as zero-order, first-order, and Korsmeyer-Peppas (KP) models, are illustrated in Fig. 6.5 B.

Table 6.1. Rate constant and linear correlation coefficient values derived from fitting the cumulative DOX release data of HA nanorods, nanoplates, and thin nanoplates.

Kinetic models	**Zero order**		**First order**		**Higuchi model**		**KP model**		
HA	**K_o**	**R^2**	**K_1**	**R^2**	**K_H**	**R^2**	**K_{Kp}**	**N**	**R^2**
Nanorods	0.1380 ± 0.0118	0.9650	0.002 ± 0.0002	0.9680	1.3010 ± 0.16	0.9270	56.90 ± 1.023	0.0440 ± 0.007	0.8790
Nanoplates	0.0850 ± 0.0195	0.8650	0.001± 0.0003	0.8640	0.8830 ± 0.21	0.8520	51.50 ± 1.03	0.0370 ± 0.01	0.8120
Thin nanoplates	0.1280 ± 0.0153	0.9210	0.002 ± 0.0003	0.9190	1.2090 ± 0.10	0.9600	42.60 ± 1.01	0.0520 ± 0.04	0.9660

6.3. Cytocompatibility

Fig. 6.6 A illustrates the time-dependent viability of MG-63 cells, treated with DOX-HNRs, DOX-HNPTs, and DOX-HTNPTs at increasing concentrations of 10, 100 and 200 µg/ml. The results show that the cell viability is found to be increased with incubation time. Notably, all DOX-HA nanocrystals samples exhibited better cell viability compared to the PBS control, indicating their ability to support cell growth with minimal DOX toxicity, attributed to the biocompatible nature of HA nanocrystals. This is also supported by our previous research data [10]. The concentration and shape of DOX-HA nanocrystals are observed to affect cell behavior. At the highest concentration of 200 µg/ml, a slight reduction in cell viability was observed, likely due to the increased amount of loaded DOX causing some adverse effects. Rok et al.[11] and Hadjimichael et al.[12] also revealed the toxic effect of DOX on cell functions. It significantly inhibited the cell growth and proliferation. Among the different morphological DOX-HA nanocrystals samples, DOX-HTNPTs showed lower cell viability as compared to DOX-HNPTs and DOX-HNRs. Such difference in their cell viability reflects two possibilities. First, it might be the effect of varied morphologies of HA nanocrystals as our previous study demonstrated the degree of cell growth on HA nanorods, nanoplates, and thin

nanoplates in descending order [16]. Second, it might be the result of increased in the degree of DOX loading and their sustained release response from HA nanorods, nanoplates, and thin nanoplates.

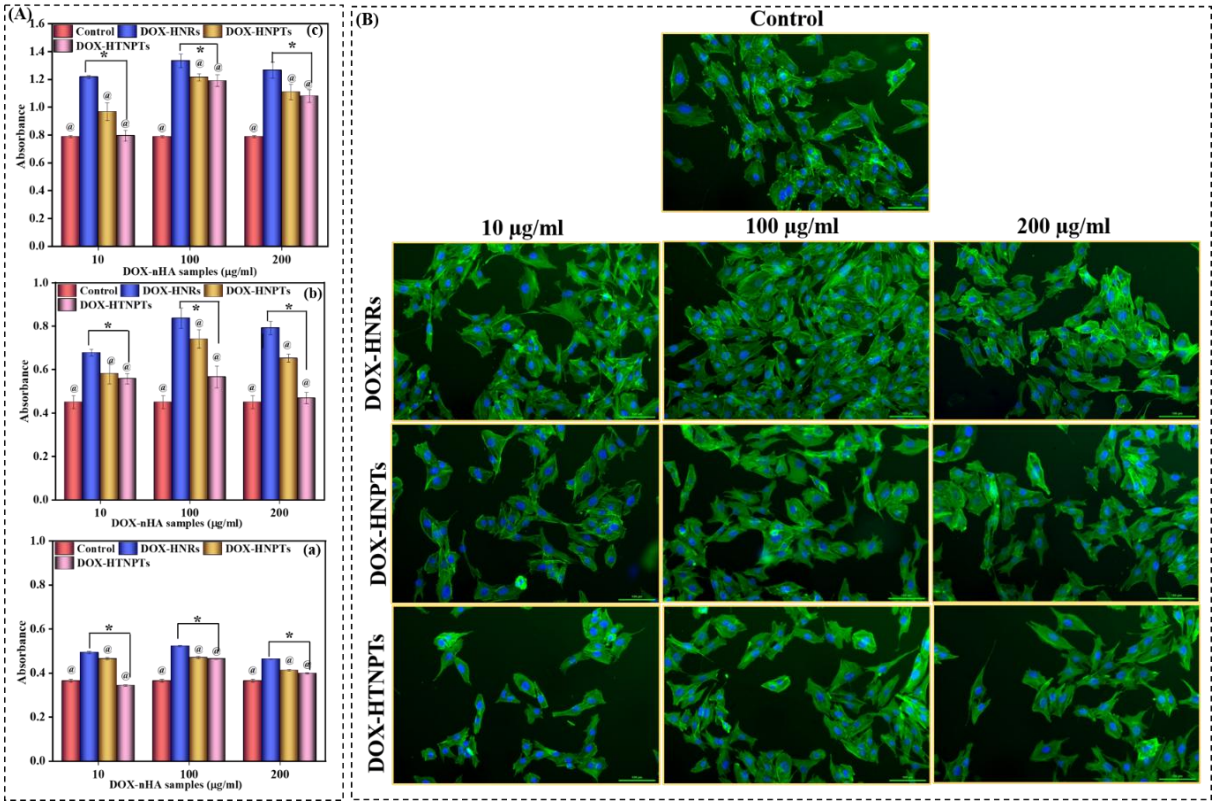

Figure 6.6 *(A) Viability of MG-63 cells on DOX-HNRs, DOX-HNPTs, and DOX-HTNPTs after incubation period of 24 (a), 48 (b), and 72 h (c). (B) Fluorescence images (Scale bar: 100 µm), showing the adhered cells on DOX-HNRs, DOX-HNPTs, DOX-HTNPTs, and control after incubation period of 72 h.*

The cytocompatibility of DOX-HA nanocrystals samples was also assessed qualitatively through fluorescence microscopy imaging of MG-63 cells after 3 days of culture. From Fig. 6.6 B, adherent cells exhibit a more flattened polygonal morphology on DOX-HNRs and DOX-HNPTs as compared to the control. In contrast, cells adhered to DOX-HTNPTs are slightly shranked across all concentrations. However, at higher concentrations (100 and 200 µg/ml), the cell spreading area on DOX-HTNPTs is comparable to the control. These results indicate that all the developed DOX-HA nanocrystals samples support favorable cell adhesion at

elevated concentrations. Notably, the spreading area of adhered cells follow a decreasing trend in the order of DOX-HNRs > DOX-HNPTs > DOX-HTNPTs, which is particularly evident at the 10 µg/ml concentration. A similar trend in cell viability across these samples was also observed in the MTT assay result.

6.4. Hemocompatibility

Fig. 6.7A illustrates the hemolysis plot, showing the percentage of RBCs damage after treatment with DOX-HA nanocrystals samples, including DOX-HNRs, DOX-HNPTs, and DOX-HTNPTs, at varying concentrations (10, 100, and 200 µg/ml). In all the cases, RBCs damage remained below 5 %, indicating good hemocompatibility according to the ASTM-F756-00 standard. Among the different DOX-HA nanocrystals samples, DOX-HNRs caused the highest hemolysis, particularly at lower concentrations, compared to DOX-HNPTs and DOX-HTNPTs. However, pure DOX did not significantly damage RBCs. The variation in hemolysis (%) among DOX-HA nanocrystals samples can be attributed to the differences in HA nanocrystals shapes. Our previous research also found that HA nanorods caused more RBC damage [10]. These variations in hemolysis (%) among HA nanorods, nanoplates, and thin nanoplates were linked to surface charge differences. HA nanorods, with a less negative surface charge (– 6.1 mV), exhibit stronger interactions with the negatively charged RBCs membranes, resulting in more significant cell membrane disruption compared to HA nanoplates (– 44.2 mV), and thin nanoplates (– 48.1 mV).

6.5. Antibacterial activity

Fig. 6.7B presents a MTT plot, representing viability of *S. aureus* bacteria, treated with DOX-HNRs, DOX-HNPTs, DOX-HTNPTs, and pure DOX (positive control) at increasing concentrations of 10, 100 and 200 µg/ml. Results clearly demonstrate the significant antibacterial activity of DOX-HA nanocrystals samples at all concentrations, as less bacterial viability is observed on all samples compared to negative control (PBS). The bacterial viability

in DOX-HNPTs and DOX-HTNPTs was less than bacteria treated with DOX alone. The sustained release of DOX from HA nanoplates and thin nanoplates allow their sufficient amount to reach the bacteria owing to good bio-availability [13, 14]. However, burst release (62 % in 8 h) of DOX from HA nanorods killed the less number of bacteria as compared to DOX-HNPTs and DOX-HTNPTs. Even the bacterial viability of DOX-HNRs is higher than pure DOX at all the concentrations. Unlike HA nanorods and nanoplates, the delayed release of DOX from HA thin nanoplates made the bacteria least viable, revealing their higher antibacterial response as compared to all the developed DOX-HA nanocrystals and positive and negative controls.

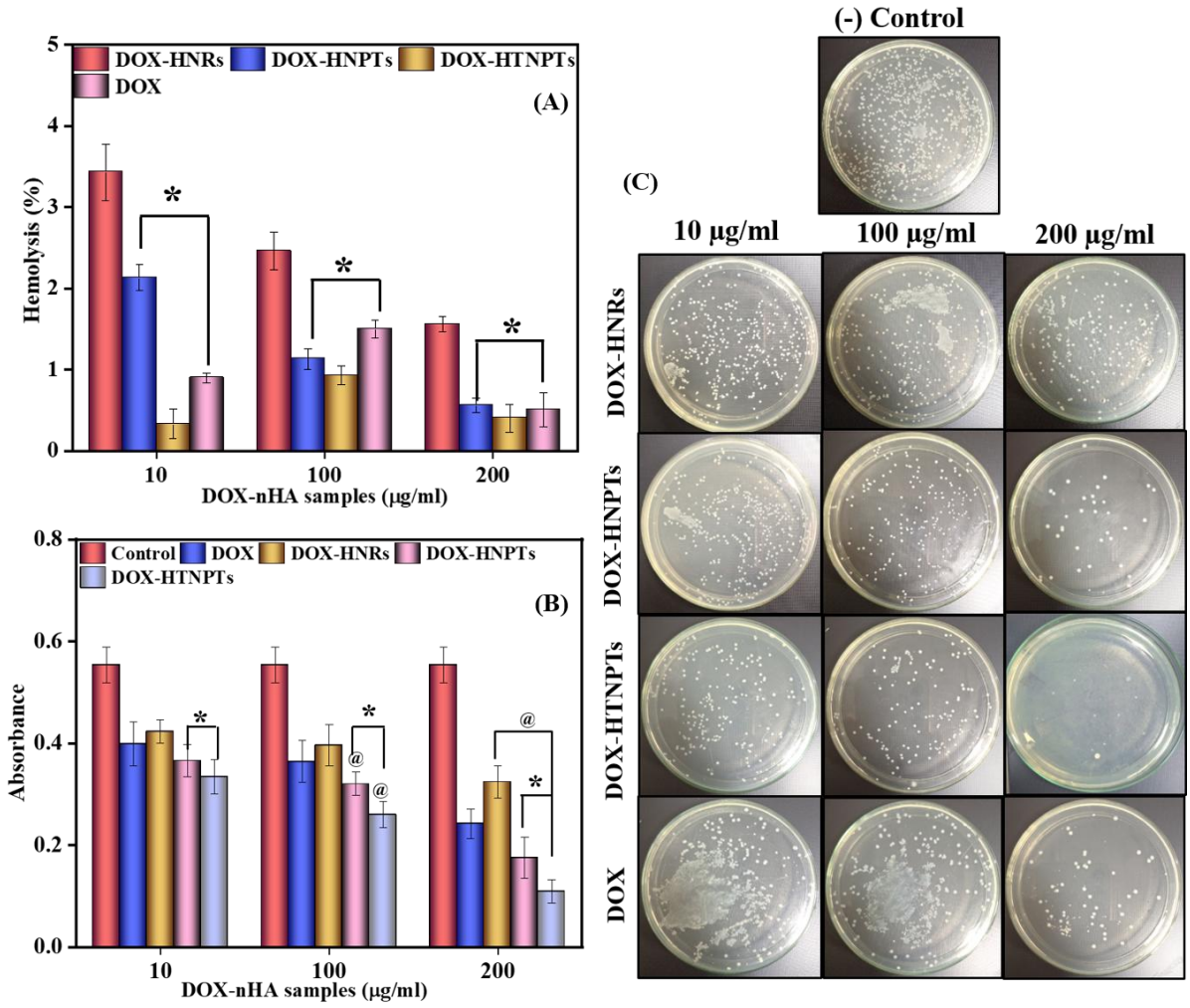

Figure 6.7 *(A) Hemolysis (%) plot, showing the lysed RBCs after treating with 10, 100 and 200 µg/ml concentrated DOX-HA nanocrystals samples. Standard deviation values were obtained from three independent experiments with $p \leq 0.05$, where (*) denotes a significant difference in the mean hemolysis values of DOX-HNPTs, DOX-HTNPTs, and pure DOX compared to DOX-HNRs (B) MTT plot, illustrating the viability of S. aureus bacteria on DOX-HNRs, DOX-HNPTs, DOX-HTNPTs, and pure DOX. Value of standard deviation was obtained from three independent experiments, at $p \leq 0.05$, and (C) Digital images of bacterial colonies developed on agar plates after treatment with DOX-HNRs, DOX-HNPTs, DOX-HTNPTs, and pure DOX.*

For qualitative evidence, the bacterial viability on DOX-HA nanocrystals was also assessed using colony-counting method (Fig. 6.7 C) and live-dead assay (Fig. 6.8). Significantly reduced

number of bacterial colonies has been formed on agar plates for all DOX-HA nanocrystals samples compared to negative control. It is also well matched with fluorescence images as higher number of *S. aureus* bacteria is visible on negative control. In case of DOX-HNRs, the slightly similar and high number of bacterial-colonies has been observed at all concentrations due to burst release of DOX. In contrast, formation of bacterial colonies is inversely proportional to samples concentrations for DOX-HNPTs, DOX-HTNPTs, and pure DOX. Due to sustained release of DOX from HA nanoplates and thin nanoplates, growth of treated bacteria is even more highly controlled as compared to pure DOX. Limited bacterial colonies are formed on DOX-HTNPTs. Similar case is also observed in fluorescence images. Most of the bacteria are dead on DOX-HTNPTs. Overall, these results reveal the antibacterial potential of sustained released DOX from HA thin nanoplates.

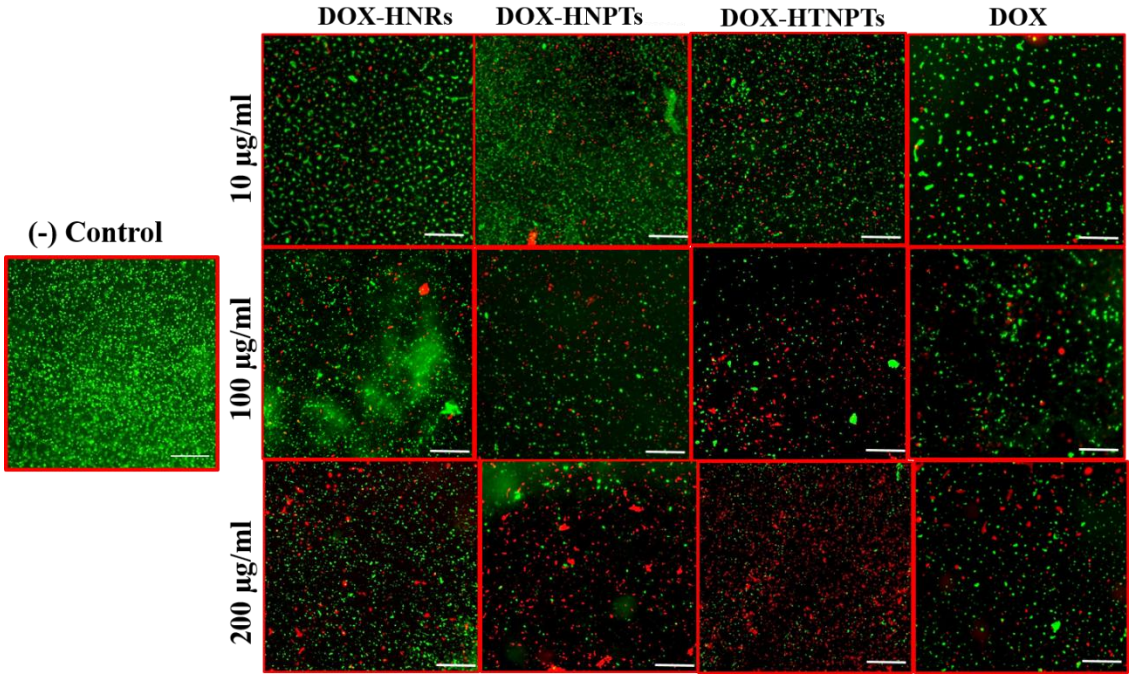

Fig. 6.8 *Fluorescence images (Scale bar: 100 µm), showing the stained live (green) and dead (red) bacterial cells on similar samples.*

6.6. Summary

This study investigates the potentiality of HA nanoplates as a novel drug vehicle for sustained delivery of DOX to eradicate the bacterial infection in comparison to HA nanorods (Fig. 6.9). The DOX loading efficiencies of HA nanorods, nanoplates, and thin nanoplates were evaluated to be 45.5, 62.2, and 73.3 %, respectively. The successful DOX loading was confirmed through FTIR and XRD, while morphological changes before and after DOX loading was also revealed by FESEM and TEM. Among the tested samples, HA thin nanoplates showed the most prolonged DOX release profile, releasing 51 % of DOX within 48 h, followed by HA nanoplates and HA nanorods which showed release profiles of 59.5 and 68 % in 48 h, respectively. The differential DOX loading and release rate as per shape of HA nanocrystals was thoroughly explained on the basis of surface area of HA and their nature of interaction with DOX. *In vitro* cell culture studies demonstrated that DOX-HA nanocrystals formulations effectively promoted cell adhesion and proliferation, with DOX-HNRs, DOX-HNPTs, and DOX-HTNPTs exhibiting cell viability in decreasing order. The relatively lower viability observed for DOX-HTNPTs was attributed to their highest DOX loading efficiency and sustained drug release profile. Additionally, Hemolysis studies also confirmed all DOX-HA nanocrystals possess good hemocompatibility (< 5% RBC lysis). Furthermore, *in vitro* antibacterial studies revealed that, unlike HA nanorods and free DOX, the prolonged DOX release from HA thin nanoplates leads to nearly complete bacterial inhibition at a concentration of 200 µg/ml (Fig. 6.9). These findings suggest that among the different HA nanocrystals morphologies, HA thin nanoplates hold the greatest potential as a sustained antibiotic drug vehicle for effective bacterial eradication in the treatment of Osteomyelitis.

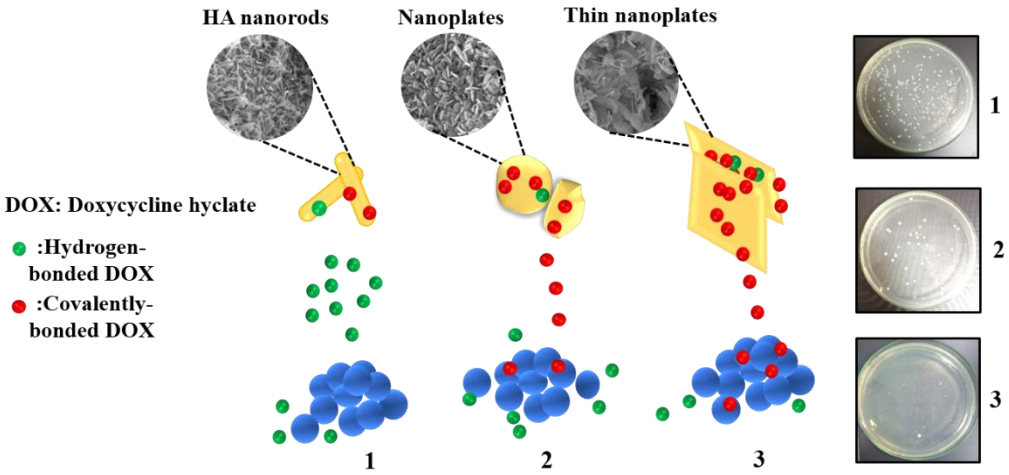

Fig. 6.9 *Graphical representation of the bactericidal effects of DOX-loaded different morphological HA nanocrystals*

References

[1] F. Zheng, S. Wang, M. Shen, M. Zhu, X. Shi, Antitumor efficacy of doxorubicin-loaded electrospun nano-hydroxyapatite–poly(lactic-co-glycolic acid) composite nanofibers, Polymer Chemistry 4(4) (2013) 933-941.

[2] N.-I. Farkas, L. Marincaș, R. Barabás, L. Bizo, A. Ilea, G.L. Turdean, M. Toșa, O. Cadar, L. Barbu-Tudoran, Preparation and Characterization of Doxycycline-Loaded Electrospun PLA/HAP Nanofibers as a Drug Delivery System, Materials, 2022.

[3] M. Mateescu, S. Doncea, I. Chican, C. Nistor, I. Bujanca, Synthesis of Calcium Carbonate Micro Particles using Emulsion Membrane Process Applied for Drug Release Studies, Revista de Chimie 68 (2017) 2320-2324.

[4] H. Wang, L. Zhao, X. Yu, S. Lei, Y. Qi, C. Cui, Synthesis of silver modified hydroxyapatite nanoparticle and evaluation of its biological properties in vitro for potential biomedical application, Journal of the Ceramic Society of Japan 129(7) (2021) 443-452.

[5] R. Soria-Martínez, M. Longuinho, A.M. Rossi, Non-covalent interactions and adsorption affinities of doxycycline and tetracycline with the (010) and (001) surfaces of hydroxyapatite. A DFT and experimental study, Surfaces and Interfaces 46 (2024) 104010.

[6] J.S. Stevens, S.J. Byard, C.C. Seaton, G. Sadiq, R.J. Davey, S.L.M. Schroeder, Proton transfer and hydrogen bonding in the organic solid state: a combined XRD/XPS/ssNMR study of 17 organic acid–base complexes, Physical Chemistry Chemical Physics 16(3) (2014) 1150-1160.

[7] S.J. Kerber, J.J. Bruckner, K. Wozniak, S. Seal, S. Hardcastle, T.L. Barr, The nature of hydrogen in x-ray photoelectron spectroscopy: General patterns from hydroxides to hydrogen bonding, Journal of Vacuum Science & Technology A 14(3) (1996) 1314-1320.

[8] M. Bin Mobarak, M.N. Islam, F. Chowdhury, M.N. Uddin, M.S. Hossain, M. Mahmud, U.S. Akhtar, N.I. Tanvir, A.F.M.M. Rahman, S. Ahmed, Calcined chicken eggshell-derived

biomimetic nano-hydroxyapatite as a local drug-delivery aid for doxycycline hyclate: characterization, bio-activity, cytotoxicity, antibacterial activity and in vitro release study, RSC Advances 13(51) (2023) 36209-36222.

[9] C. Soriano-Souza, H. Valiense, E. Mavropoulos, V. Martinez-Zelaya, A.M. Costa, A.T. Alves, M. Longuinho, R. Resende, C. Mourão, J. Granjeiro, M.H. Rocha-Leao, A. Rossi, M. Calasans-Maia, Doxycycline containing hydroxyapatite ceramic microspheres as a bone-targeting drug delivery system, Journal of biomedical materials research. Part B, Applied biomaterials 108(4) (2020) 1351-1362.

[10] U. Kesarwani, A.K. Dubey, Cytocompatibility and osteogenic response of 1- and 2-dimensional (D) nanostructured hydroxyapatite: Influence of surface chemistry, ion release and hydrophilicity, Inorganic Chemistry Communications 173 (2025) 113824.

[11] J. Rok, M. Karkoszka, Z. Rzepka, M. Respondek, K. Banach, A. Beberok, D. Wrześniok, Cytotoxic and proapoptotic effect of doxycycline - An in vitro study on the human skin melanoma cells, Toxicology in vitro : an international journal published in association with BIBRA 65 (2020) 104790.

[12] A.C. Hadjimichael, A.F. Foukas, E. Papadimitriou, A. Kaspiris, C. Peristiani, I. Chaniotakis, M. Kotsari, A. Pergaris, S. Theocharis, P. Sarantis, M. Christopoulou, A. Psyrri, A.F. Mavrogenis, O.D. Savvidou, P.J. Papagelopoulos, A. Armakolas, Doxycycline inhibits the progression of metastases in early-stage osteosarcoma by downregulating the expression of MMPs, VEGF and ezrin at primary sites, Cancer treatment and research communications 32 (2022) 100617.

[13] A.P.S. Prasanna, G.D. Venkatasubbu, Sustained release of amoxicillin from hydroxyapatite nanocomposite for bone infections, Progress in biomaterials 7(4) (2018) 289-296.

[14] S.V. Gopala Kumari, N.A. Manikandan, K. Pakshirajan, G. Pugazhenthi, Sustained drug release and bactericidal activity of a novel, highly biocompatible and biodegradable polymer nanocomposite loaded with norfloxacin for potential use in antibacterial therapy, Journal of Drug Delivery Science and Technology 59 (2020) 101900.